PAPER

Check for updates

Three-dimensional tellurium and nitrogen Co-doped mesoporous carbons for high performance supercapacitors†

Chang Ki Kim,‡ Jung-Min Ji,‡ M. Aftabuzzaman [ID] and Hwan Kyu Kim [ID] *

Tellurium-doped mesoporous carbon composite materials (Te/NMC) have been prepared by a facile intercalation method in the presence of nitrogen-doped mesoporous carbon (NMC) with tellurium powder, for the first time. The effects of the co-doped N and Te in the mesoporous carbon matrix on the physical/chemical properties and capacitance performances were investigated *via* the use of various characterization methods and electrochemical studies. The as-prepared NMC and Te/NMC materials were found to mainly be composed of mesopores and maintained the 3D hierarchical graphite-like structure with lots of defect sites. By intercalation of Te atoms into the NMC materials, 2.12 at% (atom%) of Te was doped into NMC and the specific surface area of Te/NMC ($261.07 \ m^2 \ g^{-1}$) decreased by about 1.5 times compared to that of NMC ($437.96 \ m^2 \ g^{-1}$). In electrochemical measurements as a supercapacitor (SC) electrode, the Te/NMC based electrode, even with its lower porosity parameters, exhibited a higher capacitive performance compared to the NMC-based electrode. These results for Te/NMC arise due to the pseudo-capacitive effect of doped Te and the increase in the capacitive area available from the formation of interconnections in the mesoporous carbons through Te−O bonds. As a result, the synergetic effect of the Te and N atoms enables Te/NMC to exhibit the highest specific capacitance of $197 \ F \ g^{-1}$ at a current density of $0.5 \ A \ g^{-1}$. Moreover, remarkable long-term cycling stability with the retention of more than 95% of the initial capacitance is observed for Te/NMC at a current density of $5 \ A \ g^{-1}$ and also for 1000 charge−discharge cycles.

1. Introduction

With the increasing global energy demand and environmental concerns, renewable energy sources, including sunlight, wind, hydro, hydrogen and geothermal heat, have been considered as promising alternatives to fossil fuels.[1–3] Accordingly, many researchers have devoted huge efforts to renewable energy sources in terms of energy generation, storage, and conservation technologies.[4–8] Among these technologies, electric energy storage (EES) technologies have become an urgent requirement for efficient energy management due to the large fluctuations in renewable energy generation, as well as a necessity in our daily life.[7,9,10]

As one of the EES technologies, electrochemical capacitors, *i.e.* supercapacitors (SCs), have attracted considerable attention because of their remarkable power performance, long-term cycling stability ($>10^6$ cycles), low maintenance costs, ease of integration into electronics and good safety.[11] Their advantages

arise from their charge storage mechanisms, which can be generally classified into two categories: (i) electric double layer capacitance (EDLC) and (ii) pseudocapacitance (PC).[12,13] EDLCs electrostatically store charge by forming a Helmholtz double layer at the interface between the electrode and electrolyte, *i.e.*, a non-faradaic process occurs,[14] while PCs faradaically store charge *via* reversible electrochemical reactions on the surface of redox-active materials, *i.e.*, a faradaic process occurs. In practice, the EDLC and PC mechanisms coexist in SCs, contributing in different proportions.[15] According to each mechanism, the specific capacitance (C_S) of an EDLC depends on the accessible surface area and properties of the electrode materials, and the C_S of a PC is strongly related to the valence state change of the redox-active materials.[16] Many electro-active materials, such as conducting polymers,[17,18] metal oxides,[19–21] noble metals[22] and carbons,[12] and preparation methods[23–25] have been developed and tested for more efficient supercapacitors.[26] Among them, carbon-based materials, such as commercial active carbons,[14,27] carbon nanomaterials,[28,29] graphene[30–32] and templated carbons,[33,34] are the most extensively examined and studied as electro-active materials for the EDLC mechanism. This is ascribed to their high specific surface area, electrochemical stability, and open porosity to electrolyte ions. However, carbon-based materials have relatively low rate capability and cycling

Global GET-Future Laboratory, Department of Advanced Materials Chemistry, Korea University, 2511 Sejong-ro, Sejong 339-700, Korea. E-mail: hkk777@korea.ac.kr

† Electronic supplementary information (ESI) available: Information and details of GPC data, electrochemical measurement and the related equations are available. See DOI: 10.1039/d0ra10374h

‡ These authors contributed equally to this work.

stability, because the capacitive charge storage mainly occurs at the micropores (<2 nm).[35] Therefore, the porosity control of carbon-based materials is one of the main themes to guarantee better performance in terms of power delivery and energy storage.[35,36] However, to overcome the low capacitance performance of carbon-based materials, metal oxides and heteroatoms, such as boron,[37] nitrogen,[38,39] oxygen,[40] phosphorous[41,42] and sulfur,[43] are incorporated into the surface of carbon-based materials.[44–48] The incorporation of metal oxides and heteroatoms has led to an improvement in the capacitive performance of such materials, as shown in Table S1.†[36] In our previous study, we developed a preparation method of soft-templated nitrogen-enriched mesoporous carbon (NMC) with controlled pore size and volume as a counter electrode in dye-sensitized solar cells (DSSCs).[49,50] The preparation method was beneficial to tailoring the pore structures of carbon materials by controlling the temperature of pyrolysis and the composition of the PAN-*b*-PBA copolymer, which consists of polyacrylonitrile (PAN) as a carbon source and poly(*n*-butyl acrylate) (PBA) as a sacrificial block.[51] Based on the preparation method, very recently, we reported Ru-doped carbon materials as supercapacitor materials, which showed outstanding capacitive performance and cycling stability.[46] This can be attributed to the PC and well-organized distribution of Ru throughout the NMC.

In this study, we prepared a tellurium-doped mesoporous carbon composite material (Te/NMC), for the first time, *via* a facile intercalation method in the presence of nitrogen-doped mesoporous carbon (NMC) and tellurium powder to investigate the capacitive behaviour of tellurium and nitrogen dual-doped carbon materials. The effect of Te and N atoms on the structural properties was carefully scrutinized using various characterization methods, such as elemental analysis (XPS and EDS), Raman spectroscopy, nitrogen sorption isotherm measurements (BET), and field emission scanning electron microscopy (FE-SEM). We also demonstrate that the incorporation of Te in carbon-based nanomaterials is a good strategy to improve the capacitive performance of carbon materials and that the incorporation of two types of atoms improves the overall capacitive performance of the materials due to their synergetic effect.

2. Experimental section

2.1. Materials

n-Butyl acrylate, acrylonitrile, α,α′-azoisobutyronitrile, copper(II) bromide, tris(2-pyridylmethyl)amine, 2,2′-bipyridyl, ethyl α-bromoisobutyrate, copper(I)chloride, aluminium oxide, dimethyl sulfoxide, ethanol, dimethylformamide, toluene, hydrochloric acid, potassium hydroxide, methanol, and tellurium metalloid were provided by Sigma-Aldrich.

2.2. Preparation of the nitrogen-doped mesoporous carbon (NMC) material

The as-prepared block copolymer (PAN-*b*-PBA) was placed in a quartz furnace. Then, it was stabilized at 280 °C under an air atmosphere (heating rate: 5 °C min^{-1}, time: 2 h) and carbonized at 900 °C under a nitrogen atmosphere (heating rate: 5 °C min^{-1}, time: 1 h).

2.3. Preparation of the Te/nitrogen-doped mesoporous carbon composite (Te/NMC) material

The NMC material was physically mixed with tellurium powder (w/w%), and it was directly placed in a furnace. The mixture of **NMC** and tellurium powder was carbonized at 600 °C to introduce tellurium atoms into the **NMC** under a nitrogen atmosphere (heating rate: 5 °C min^{-1}, time: 1 h). The final product was washed with aqueous solutions of 1 M HCl and 3 M KOH to remove the unreacted tellurium.

3. Results and discussion

Fig. 1 shows the preparation method of the tellurium/nitrogen-doped mesoporous carbon composite (Te/NMC) material. The PAN-*b*-PBA block copolymer, which consists of a sacrificial block (PBA) and a nitrogen-enriched carbon block (PAN), was synthesized *via* the atom transfer radical polymerization (ATRP) method according to previous work.[46,49] The PAN-*b*-PBA block copolymer was characterized by gel permeation chromatography (GPC). The number-average molecular weight of the PAN-*b*-PBA copolymer was determined to be 35 200, and the copolymer composition and polydispersity index were estimated to be $(AN)_{109}$-$(BA)_{4000}$ and 1.25, respectively (Fig. S1†). To prepare the nitrogen-doped mesoporous carbon (**NMC**), the PAN-*b*-PBA block polymer was stabilized and carbonized in a furnace, according to previous reports.[35–37] The prepared **NMC** was then mixed with tellurium powder (1 : 1 w/w%). After that, the mixture was carbonized to intercalate the tellurium atoms into the carbon network. The **Te/NMC** was simply prepared using the carbon source and tellurium precursor. The detailed preparation methods are given in the Experimental section.

Fig. 1 Preparation method of the tellurium/nitrogen-doped mesoporous carbon composite material.
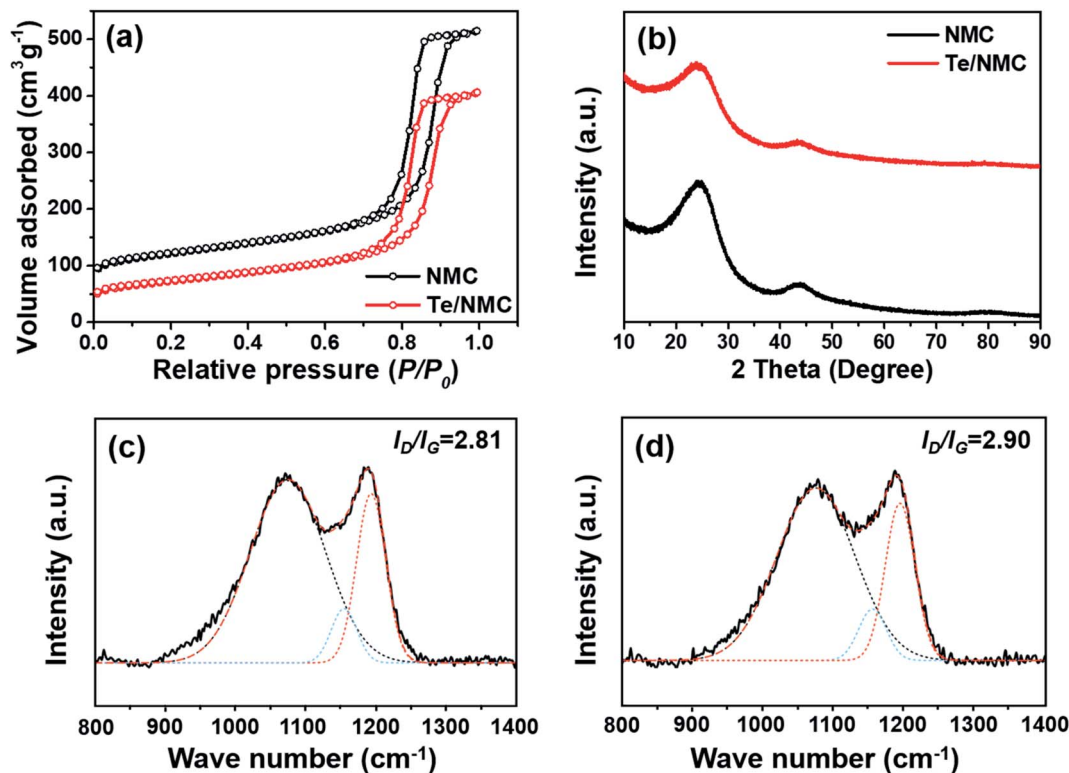
Fig. 2 (a) Nitrogen adsorption–desorption isotherms, (b) XRD diffraction patterns and Raman spectra of (c) NMC and (d) Te/NMC.

To investigate the specific surface area and porosity of **NMC** and **Te/NMC**, nitrogen sorption isotherm measurements were conducted. The nitrogen adsorption–desorption isotherm plots of **NMC** and **Te/NMC** are displayed in Fig. 2a, and the parameters are tabulated in Table 1. As shown in Fig. 2a, the isotherm plots of both **NMC** and **Te/NMC** exhibit type IV isotherms with a H1 hysteresis loop. This indicates a well-developed mesopore and inter-connected pore carbon structure. The specific surface areas of the **NMC** and **Te/NMC** materials were calculated to be 437.96 and 261.07 m^2 g^{-1} with total pore volumes of 0.80 and 0.63 cm^3 g^{-1}, respectively. The pore sizes were estimated to be 11.28 and 11.37 nm for **NMC** and **Te/NMC**, respectively. Interestingly, despite the surface areas and total pore volumes of **Te/NMC** being lower than those of **NMC**, the pore sizes of **NMC** and **Te/NMC** are almost the same. This indicates that the Te metalloid was intercalated into the **NMC** well and does not block the inner-pores of the **NMC**.

To assess the structural characteristics of the two carbon materials, X-ray diffraction (XRD) measurements and Raman spectroscopy were carried out (Fig. 2b–d). Fig. 2b displays the

XRD patterns of the two materials. These patterns show broad diffraction peaks at 25° and 43°, which correspond to the (002) and (100) planes of graphitic carbon, indicating their amorphous and disordered structures.[51,52] However, there are no crystal peaks for Te, indicating the atomically dispersed Te in the carbon network. Fig. 2c and d display the Raman spectra of **NMC** and **Te/NMC**, respectively. The spectra for both materials exhibit three distinct peaks at around 1350, 1590, and 1510 cm^{-1}, which are assigned to the defect-induced band (D), in-plane vibrational graphitic-induced band (G), and amorphous structure band (A) of carbon, respectively.[53] In general, it is well known that the D band becomes active as a result of defects occurring in the carbon lattice from the Raman inactive mode (A$_{1g}$), and the G band (E$_{2g}$) presents as a result of the stretching vibration mode of the C–C bond. Therefore, the intensity ratio of the D and G bands (I_D/I_G) in carbon materials is often used to estimate the level of disorder in graphitic structures.[54,55] The I_D/I_G ratios for **NMC** and **Te/NMC** were determined to be 2.81 and 2.90, respectively, which implies that

Table 1 Porous properties of the NMC and Te/NMC materials[a]

Sample	S_{BET} (m^2 g^{-1})	V_{total} (cm^3 g^{-1})	V_{micro} (cm^3 g^{-1})	V_{meso} (cm^3 g^{-1})	Pore size (nm)
NMC	437.96	0.80	0.10	0.68	11.28
Te/NMC	261.07	0.63	0.03	0.60	11.37

[a] S_{BET}: BET surface area, V_{total}: total pore volume, V_{micro}: micropore volume, V_{meso}: mesopore volume.

both of the as-prepared materials contain semi-graphitic carbon with many defect sites.[54]

To observe the surface morphology and porous structure of **NMC** and **Te/NMC** materials, field emission scanning electron microscopy (FE-SEM) measurements were conducted. The SEM images at high magnification exhibit the 3D bi-continuous structure of **NMC** and **Te/NMC** with mesopores (see Fig. 3a and b). In addition, the doping of elements into the samples was detected by SEM-EDS (Fig. 3c–e for **NMC** and Fig. 3f–i for **Te/NMC**). The EDS elemental mapping results of NMC display that the N (Fig. 3d) and O (Fig. 3e) atoms are uniformly distributed in the carbon matrix, while those of Te/NMC also display the homogeneous distribution of N (Fig. 3g), O (Fig. 3h) and Te (Fig. 3i) atoms in the carbon matrix. This demonstrates that Te atoms were successfully introduced into the carbon framework of **NMC**.[50,56]

X-ray photoelectron spectroscopy (XPS) was carried out to determine the elemental composition and the bonding characteristics of the C, N, O, and Te atoms in the two materials. In Fig. 4, the X-ray survey spectra indicate the presence of C, N and O atoms in **NMC**, while **Te/NMC** exhibits the presence of C, N, O and Te atoms. Their elemental composition results are
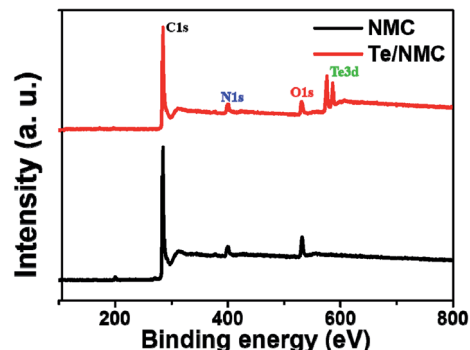

Fig. 4 XPS survey spectra of the **NMC** and **Te/NMC** materials.

summarized in Table 2. The Te content of **Te/NMC** was estimated to be approximately 2.12 atomic percentage (at%). To further understand the bonding characteristics of **NMC** and **Te/NMC**, high-resolution XPS was performed. Fig. 5 displays the bonding characteristics of the C, N, O and Te atoms. After the deconvolution of C1s for **NMC**, four major peaks were displayed at 290.8, 286.9, 285.8 and 284.6 eV that correspond to O=C–OH, –C–O,
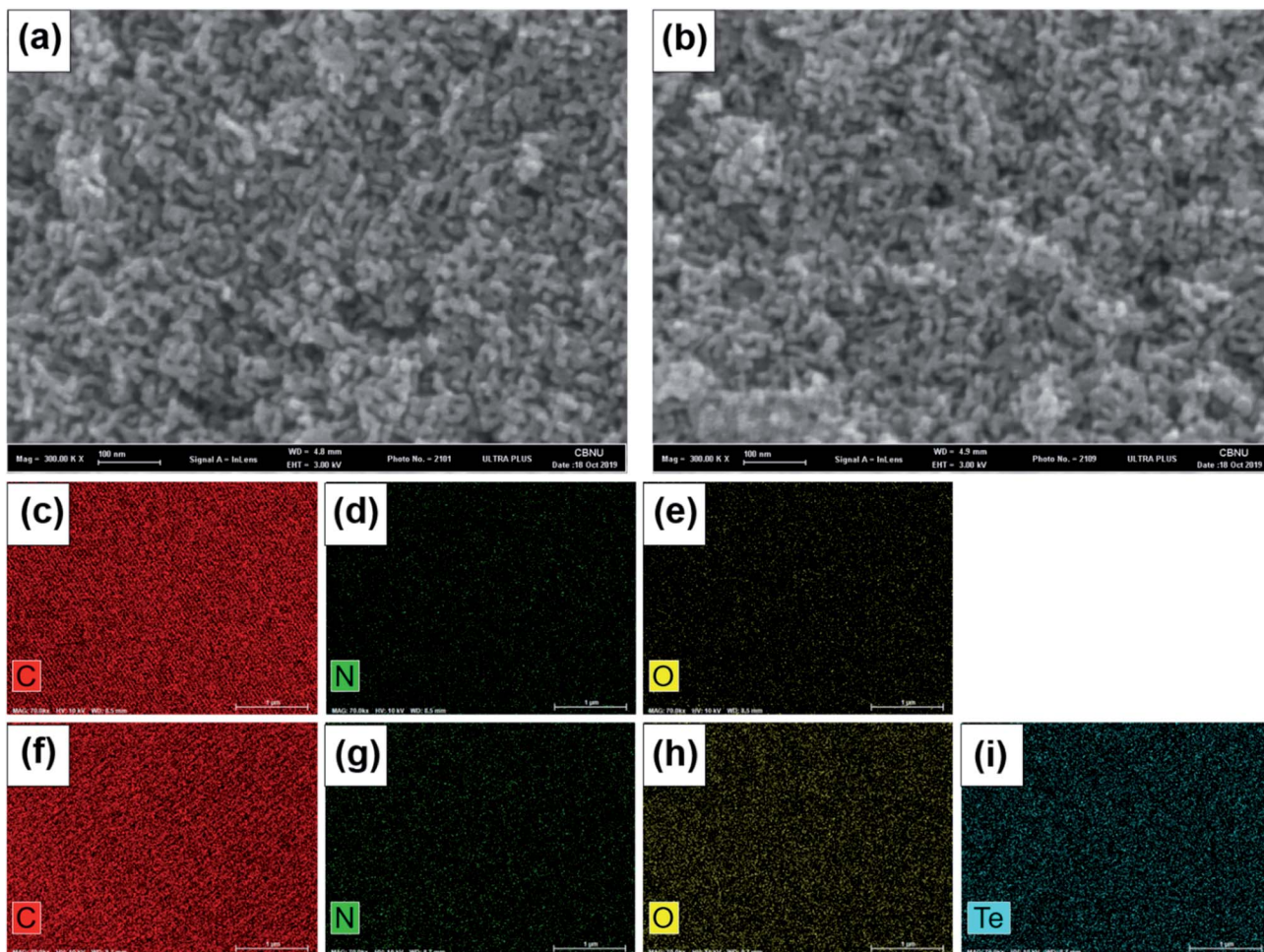

Fig. 3 (a, b) SEM images of NMC and Te/NMC at high magnification, and EDS elemental mapping of NMC ((c) carbon; (d) nitrogen; (e) oxygen) and Te/NMC ((f) carbon; (g) nitrogen; (h) oxygen; (i) tellurium).

Table 2 Elemental compositions of the NMC and Te/NMC materials

Sample	Element (at%)			
	C	O	N	Te
NMC	86.31	7.23	5.41	—
Te/NMC	85.04	5.86	6.99	2.12

–C=N/–C–N and –C–C/–C=C bonding, respectively (Fig. 5a).[57] Meanwhile, after the deconvolution of C1s for **Te/NMC**, there were five peaks: four peaks at 290.8, 286.9, 285.8 and 284.6 eV

corresponding to O=C–OH, –C–O, –C=N/–C–N and –C–C/–C=C bonding, respectively, and another peak at around 283 eV corresponding to C–Te bonding (Fig. 5d). Deconvolution of the N1s spectra of **NMC** and **Te/NMC** led to four different peaks being displayed, which are consistent with pyridinic-N (397.9 eV), pyrrolic-N (400.2 eV), graphitic-N (400.6 eV), and pyridinic-N oxide (402.3 eV), as shown in Fig. 5b and e.[58] The charge-transfer ability and overall wettability were improved by the N-heteroatoms (mainly pyridinic-N and graphitic-N) incorporated into the carbon matrix, enhancing the PC. The high-resolution O1s spectrum of **NMC** deconvoluted into two peaks at around 533.9 and 531.6 eV, which can be assigned to C–O–R and –C=O
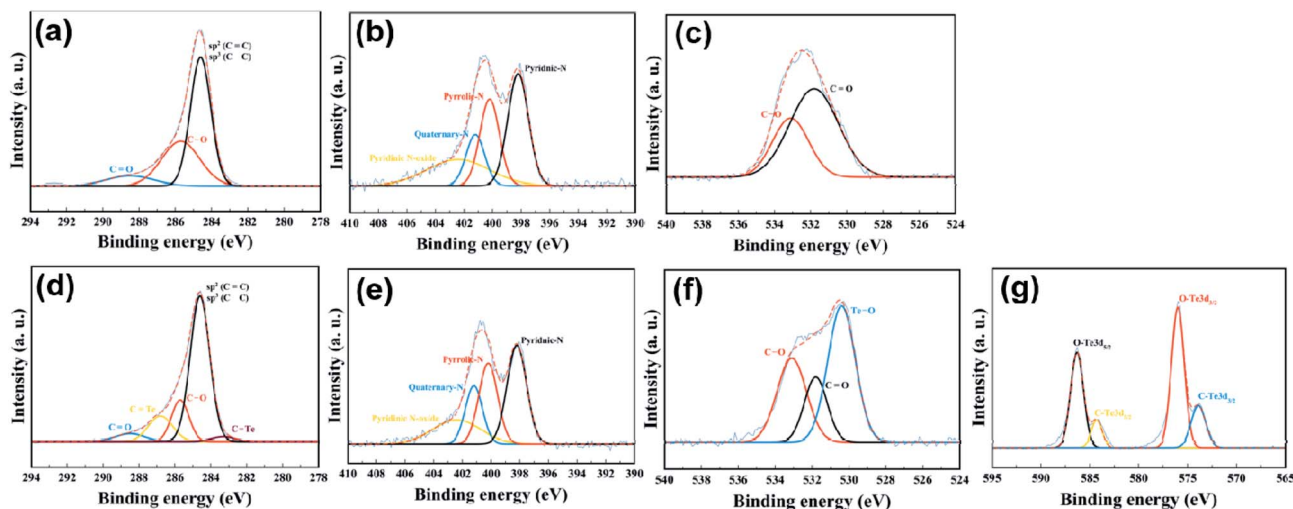

Fig. 5 High-resolution deconvoluted XPS spectra of NMC ((a) carbon, (b) nitrogen, (c) oxygen) and Te/NMC ((d) carbon, (e) nitrogen, (f) oxygen, (g) tellurium).
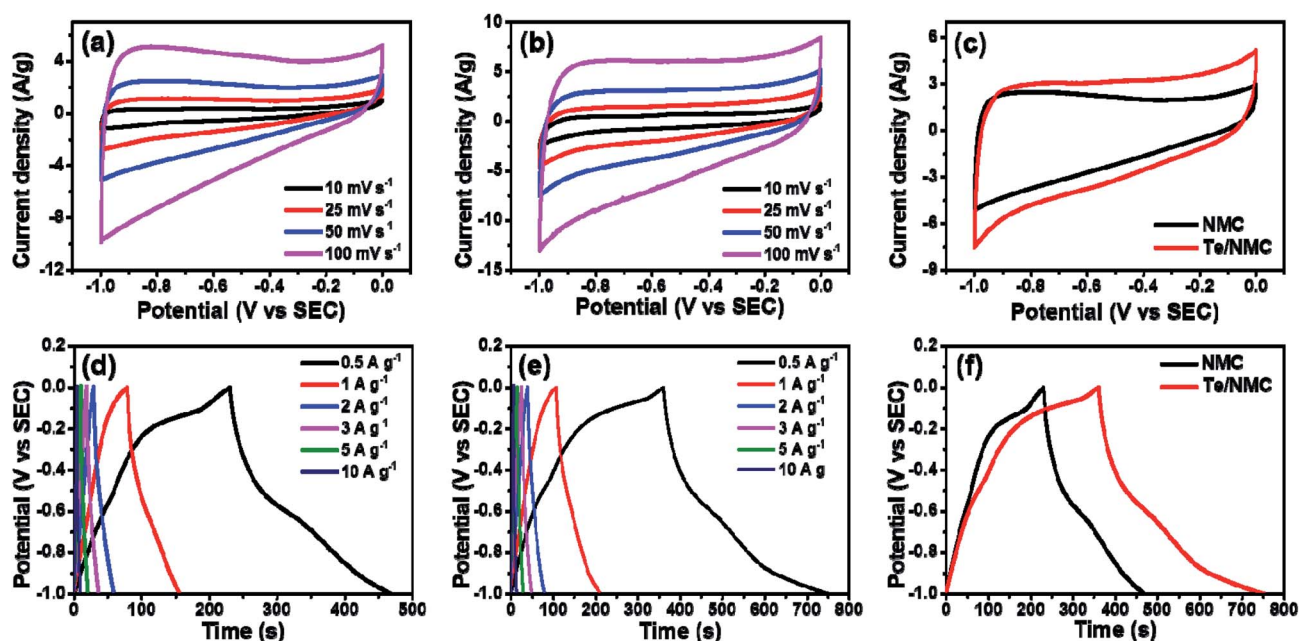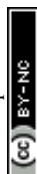

Fig. 6 CV plots of (a) NMC and (b) Te/NMC at scan rates in the range of 10–100 mV s^{-1}, (c) comparative CV plots of NMC and Te/NMC at a scan rate of 50 mV s^{-1}. GCD plots of (d) NMC and (e) Te/NMC at a current density of 0.5–10 A g^{-1}, and (f) comparative GCD plots at a scan rate of 0.5 A g^{-1}.

bonds, respectively (Fig. 5c), while those of **Te/NMC** deconvoluted into three peaks at around 534.8, 532.6 and 530.8 eV, which are consistent with to C–O–R, C=O and O–Te bonds, respectively (Fig. 5f).[51] Deconvolution of the Te3d spectrum of **Te/NMC** displays four peaks (Fig. 5g). Two of the peaks at around 586.2 and 575.9 eV, can be characterized as two splitting orbitals, $3d^{5/2}$ and $3d^{3/2}$, of the Te–O bond.[56] The other two peaks, at around 584.2 and 573.8 eV, are characterized as the splitting orbitals, $3d^{5/2}$ and $3d^{3/2}$, of the Te–C bond. Interestingly, the intensities of the Te–O bond peaks are much greater than those of the Te–C bond peaks. This can be explained by the Te atoms being intercalated with a Te–O bond rather than by a Te–C bond in the carbon matrix.[49]

The electrochemical performances of the **NMC** and **Te/NMC** electrodes were investigated in 6 M KOH electrolyte using a three-electrode system containing an Ag/AgCl reference electrode (Fig. 6). The cyclic voltammetry (CV) plots were recorded at different scan rates from 10 to 100 mV s^{-1} over a potential window of −1.0 to 0 V. The CV plots of **NMC** display a typical quasi-rectangular-like shape with a bulge. This is assigned to the N of the porous carbon (Fig. 6a).[54,55] This slight bulge at around −0.85 V indicates the presence of PS with EDLC, which is associated with the electrochemical reaction of the doped nitrogen functional group. Moreover, a quasi-rectangular-like shape after increasing the scan rate from 10 to 100 mV s^{-1} was observed in the CV plots, which indicates a fast charge transfer rate and facile ion passage within the **NMC** electrodes. In the case of **Te/NMC** (see Fig. 6b), the CV plots of **Te/NMC** are similar to those of the **NMC**, but they exhibit a slightly broadened PC peak with increasing current density compared to the **NMC** electrodes. This represents the PC intensification as a result of the incorporation of Te atoms and the increase in the capacitive area available as a result of the formation of interconnections in the mesoporous carbons through Te–O bonds.[44]

The gravimetric capacitances (*i.e.*, C_S) of the electrodes were measured by carrying out galvanostatic charge–discharge (GCD) measurements at different current densities (0.5, 1, 2, 3, 5, and 10 A g^{-1}). The C_S values were estimated using the equation $C_S = I \times \Delta t/m \times \Delta V$, where I is the current, Δt the discharging time, m the mass of the active material, and ΔV is the potential window. In general, the symmetric charge–discharge plots of the electrodes indicate the reversible behavior of surface redox

reactions. Fig. 6d and e display the symmetric GCD plots of **NMC** and **Te/NMC** at current densities of 2–10 A g^{-1}, but at the current densities of 0.5 and 1 A g^{-1} bent GCD plots are observed. These phenomena can be explained due to the PC that arises due to the incorporation of hetero-atoms and metal oxides.[35] In addition, the intercalation of Te atoms can result in a plateau in the charge–discharge plots due to the PC of N, which corresponds to the CV results. However, the charge–discharge time in the **Te/NMC** materials increased, indicating a higher C_S value *via* the PC of Te, and the limitation of accessibility of ion migration inside the pore structures by the interconnections between the mesoporous carbons through Te–O bonds (Fig. 6e). The projected C_S values for **NMC** and **Te/NMC** are 118 and 197 F g^{-1}, respectively. A comparison of the GCD plots of the two different electrodes at 0.5 A g^{-1} is presented in Fig. 6f.

Rate capability is one of the most important properties for SCs, since their main application field requires a fast charge–discharge rate and quick energy transfer.[16] Therefore, the rate capability of electrodes at different current densities (0.5, 1, 2, 3, 5, and 10 A g^{-1}) is shown in Fig. 7a. By increasing the current density from 0.5 to 10 A g^{-1}, the C_S values of both prepared **NMC** and **Te/NMC** electrodes decreased. This behaviour can also be attributed to the insufficient time for electrolyte transport into the entire pore structure and the PC of the doped elements.[54] In particular, the reduction of C_S for the **Te/NMC** electrode between a current density of 0.5 to 10 A g^{-1} is greater than that of the **NMC** electrode, which indicates the PC intensification *via* the incorporation of Te atoms and the increase in the interconnection in the mesoporous carbons through Te–O bonds. However, the retention of C_S for **Te/NMC** was significantly higher than that of **NMC** at all current densities (see Fig. 7a). To investigate the conductive and diffusion behavior of **NMC** and **Te/NMC** based electrodes, EIS was performed. The Nyquist plots of the **NMC** and **Te/NMC** electrodes are shown in Fig. 7b and were fitted with an appropriate equivalent circuit.[46] In the Nyquist plots, the intercepts on the real axis at higher frequencies indicate the equivalent series resistance (R_S), which is associated with the ohmic resistance of the electrode and electrolyte distribution resistance.[46] The arcs at the high- and mid-frequency imply the charge transfer resistance at the electrode/electrolyte interface (R_{CT}). The vertical graphs at the
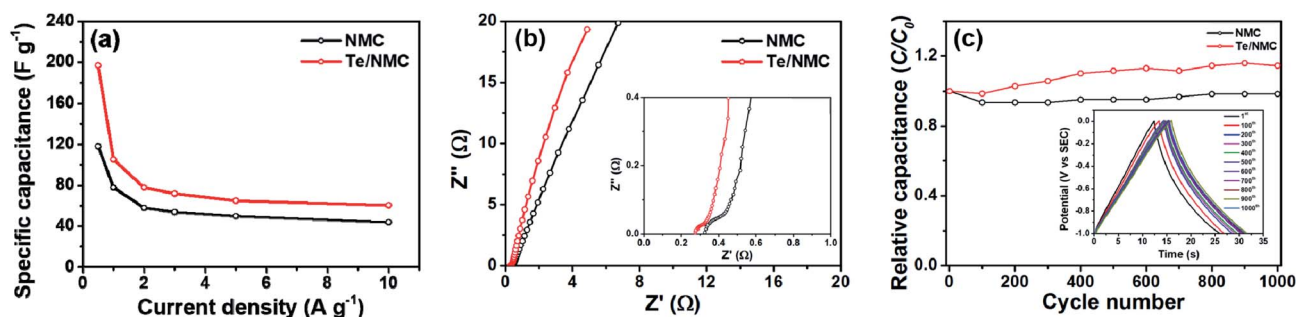

Fig. 7 (a) Rate capability of **NMC** and **Te/NMC** electrodes. (b) EIS plots of **NMC** and **Te/NMC**. (c) Cycling stability of **NMC** and **Te/NMC** at a current density of 5 A g^{-1} for 1000 cycles. Inset: galvanostatic charge–discharge of **Te/NMC**.

low-frequency indicate the good capacitive properties. As shown in Fig. 7b, the Nyquist plots display vertical graphs for the **NMC** and **Te/NMC** electrodes, which means the good capacitive properties of the electrodes. The inset of Fig. 7b displays that the R_S values of the two electrodes are 0.35 and 0.27 Ω for the **NMC** and **Te/NMC** electrodes, respectively, as determined by estimating the vertical lines and real axis. The smaller the R_S value of the **Te/NMC** electrode can be attributed to the enhancement of charge transport in the carbon matrix by the formation of interconnected mesoporous carbons through Te–O bonds. The smaller arc of the **Te/NMC** electrode at high frequency than that of the **NMC** electrode indicates the efficient PC mechanism by the incorporation of Te atoms, because the incorporation of Te atoms can reduce the activation energy for inner-path charge transfer between the electrolyte and Te-doped carbon materials, according to the previous results.[44]

Furthermore, the cycling stability of the **NMC** and **Te/NMC** electrodes was tested in a standard three-electrode configuration *via* continuous charge–discharge measurements at a current density of 5 A g^{-1} over a potential window of −1 to 0 V. As shown in Fig. 7c, it can be observed that **NMC** and **Te/NMC** electrodes exhibit excellent retention of specific capacity for 1000 cycles. However, the phenomenon of increasing capacitance after 100 cycles may be due to increase of wettability of the electrode materials and feasible accessibility of the pores by electrolyte ions.[59] In particular, the **Te/NMC** electrode shows around 115% relative capacitance after 1000 cycles. This can be attributed to the increased capacitive area in the carbon matrix as a result of the intercalation of Te atoms.

4. Conclusions

A comprehensive study was performed for the electrochemical application of tellurium/nitrogen-dual doped carbon composite materials as SC electrodes. **NMCs** were synthesized by oxidative stabilization and the pyrolysis of the PAN-*b*-PBA copolymer. Then, the Te atoms were intercalated into the carbon network of the NMCs. The as-prepared **NMC** and **Te/NMC** materials were characterized by elemental analysis (XPS and EDS) and nitrogen sorption isotherm measurement (BET). The **Te/NMC** materials mainly consisted of mesopores and retained the 3D hierarchical graphite-like structure with many defect sites. The N and Te atoms were uniformly dispersed into the carbon matrix. The doping level of **Te/NMC** is 6.99% and 2.12% for nitrogen and tellurium, respectively. The specific surface area of the **Te/NMC** materials was determined to be 261.07 m^2 g^{-1}, which is much lower than that of NMC (437.96 m^2 g^{-1}). However, despite the surface area and total pore volume, the **Te/NMC** displayed a higher specific gravimetric capacitance of 197 F g^{-1} than that of **NMC** (112 F g^{-1}) at a current density of 0.5 A g^{-1}, when evaluated as SC electrodes. In the overall analysis, it can be found that the intercalation of Te atoms into mesoporous carbon materials leads to the PC intensification and the increase of the capacitive area available, thereby improving the capacitive performance. However, the rate capabilities of the two carbon-based electrodes were low because of insufficient time for electrolyte transport into the pore structure and

pseudo-capacitance. In contrast, they exhibited remarkable cycling stability (almost 100% retention after 1000 cycles). As a result, the prepared **Te/NMC** materials were shown to be promising electrode materials for SCs and other applications. Furthermore, the present process may provide new insight for developing carbon composite materials.

Conflicts of interest

The authors declare no competing financial interest.

References

1 S. Chu and A. Majumdar, *Nature*, 2012, **488**, 294–303.
2 J. Rogelj, M. den Elzen, N. Höhne, T. Fransen, H. Fekete, H. Winkler, R. Schaeffer, F. Sha, K. Riahi and M. Meinshausen, *Nature*, 2016, **534**, 631–639.
3 M. Z. Jacobson, *Energy Environ. Sci.*, 2009, **2**, 148–173.
4 J. Y. Kim, J.-W. Lee, H. S. Jung, H. Shin and N.-G. Park, *Chem. Rev.*, 2020, **120**, 7867–7918.
5 A. Hagfeldt, G. Boschloo, L. Sun, L. Kloo and H. Pettersson, *Chem. Rev.*, 2010, **110**, 6595–6663.
6 G. M. Joselin Herbert, S. Iniyan, E. Sreevalsan and S. Rajapandian, *Renew. Sustain. Energy Rev.*, 2007, **11**, 1117–1145.
7 Y. S. Meng, *Chem. Rev.*, 2020, **120**, 6327.
8 J.-M. Ji, H. Zhou and H. K. Kim, *J. Mater. Chem. A*, 2018, **6**, 14518–14545.
9 I. Staffell, D. Scamman, A. Velazquez Abad, P. Balcombe, P. E. Dodds, P. Ekins, N. Shah and K. R. Ward, *Energy Environ. Sci.*, 2019, **12**, 463–491.
10 K. Christopher and R. Dimitrios, *Energy Environ. Sci.*, 2012, **5**, 6640–6651.
11 X. Zhang, H. Zhang, C. Li, K. Wang, X. Sun and Y. Ma, *RSC Adv.*, 2014, **4**, 45862–45884.
12 L. L. Zhang and X. S. Zhao, *Chem. Soc. Rev.*, 2009, **38**, 2520–2531.
13 Y. Shao, M. F. El-Kady, J. Sun, Y. Li, Q. Zhang, M. Zhu, H. Wang, B. Dunn and R. B. Kaner, *Chem. Rev.*, 2018, **118**, 9233–9280.
14 Y. Zhai, Y. Dou, D. Zhao, P. F. Fulvio, R. T. Mayes and S. Dai, *Adv. Mater.*, 2011, **23**, 4828–4850.
15 R. Kötz and M. Carlen, *Electrochim. Acta*, 2000, **45**, 2483–2498.
16 X. Chen, R. Paul and L. Dai, *Natl. Sci. Rev.*, 2017, **4**, 453–489.

17 C. Peng, D. Hu and G. Z. Chen, *Chem. Commun.*, 2011, **47**, 4105–4107.

18 A. Rudge, J. Davey, I. Raistrick, S. Gottesfeld and J. P. Ferraris, *J. Power Sources*, 1994, **47**, 89–107.

19 V. Augustyn, P. Simon and B. Dunn, *Energy Environ. Sci.*, 2014, 7, 1597–1614.

20 J.-H. Jeong, J. W. Park, D. W. Lee, R. H. Baughman and S. J. Kim, *Sci. Rep.*, 2019, **9**, 11271.

21 L. Kumar, H. Chauhan, N. Yadav, N. Yadav, S. A. Hashmi and S. Deka, *ACS Appl. Energy Mater.*, 2018, **1**, 6999–7006.

22 E. Herrero, L. J. Buller and H. D. Abruña, *Chem. Rev.*, 2001, **101**, 1897–1930.

23 S. Lehtimäki, M. Suominen, P. Damlin, S. Tuukkanen, C. Kvarnström and D. Lupo, *ACS Appl. Mater. Interfaces*, 2015, **7**, 22137–22147.

24 I. P. Liu, Y.-C. Hou, C.-W. Li and Y.-L. Lee, *J. Mater. Chem. A*, 2017, **5**, 240–249.

25 S. Kulandaivalu, M. Z. Hussein, A. Mohamad Jaafar, M. A. A. Mohd Abdah, N. H. N. Azman and Y. Sulaiman, *RSC Adv.*, 2019, **9**, 40478–40486.

26 Y. Wang, Y. Song and Y. Xia, *Chem. Soc. Rev.*, 2016, **45**, 5925–5950.

27 K. Subramani, N. Sudhan, R. Divya and M. Sathish, *RSC Adv.*, 2017, **7**, 6648–6659.

28 K. Gong, F. Du, Z. Xia, M. Durstock and L. Dai, *Science*, 2009, **323**, 760–764.

29 J. Yan, T. Wei, B. Shao, F. Ma, Z. Fan, M. Zhang, C. Zheng, Y. Shang, W. Qian and F. Wei, *Carbon*, 2010, **48**, 1731–1737.

30 Z.-S. Wu, A. Winter, L. Chen, Y. Sun, A. Turchanin, X. Feng and K. Müllen, *Adv. Mater.*, 2012, **24**, 5130–5135.

31 M. P. Down, S. J. Rowley-Neale, G. C. Smith and C. E. Banks, *ACS Appl. Energy Mater.*, 2018, **1**, 707–714.

32 A. Gupta, S. Sardana, J. Dalal, S. Lather, A. S. Maan, R. Tripathi, R. Punia, K. Singh and A. Ohlan, *ACS Appl. Energy Mater.*, 2020, **3**, 6434–6446.

33 H. Jiang, P. S. Lee and C. Li, *Energy Environ. Sci.*, 2013, **6**, 41–53.

34 A. B. Fuertes, G. Lota, T. A. Centeno and E. Frackowiak, *Electrochim. Acta*, 2005, **50**, 2799–2805.

35 A. Stein, Z. Wang and M. A. Fierke, *Adv. Mater.*, 2009, **21**, 265–293.

36 X. Zhao, A. Wang, J. Yan, G. Sun, L. Sun and T. Zhang, *Chem. Mater.*, 2010, **22**, 5463–5473.

37 R. Nankya, J. Lee, D. O. Opar and H. Jung, *Appl. Surf. Sci.*, 2019, **489**, 552–559.

38 H. Zhang, M. Lu, H. Wang, Y. Lyu, D. Li, S. Sun, J. Shi and W. Liu, *Sustain. Energy Fuels*, 2018, **2**, 2314–2324.

39 D. K. Kim, S. Bong, X. Jin, K.-d. Seong, M. Hwang, N. D. Kim, N.-H. You and Y. Piao, *ACS Appl. Mater. Interfaces*, 2019, **11**, 1996–2005.

40 S. Ghosh, S. Barg, S. M. Jeong and K. Ostrikov, *Adv. Energy Mater.*, 2020, **10**, 2001239.

41 Z. Bi, L. Huo, Q. Kong, F. Li, J. Chen, A. Ahmad, X. Wei, L. Xie and C.-M. Chen, *ACS Appl. Mater. Interfaces*, 2019, **11**, 11421–11430.

42 Y.-G. Lee and G.-H. An, *ACS Appl. Mater. Interfaces*, 2020, **12**, 41342–41349.

43 Z. Song, H. Duan, L. Li, D. Zhu, T. Cao, Y. Lv, W. Xiong, Z. Wang, M. Liu and L. Gan, *Chem. Eng. J.*, 2019, **372**, 1216–1225.

44 A. P. Alegaonkar, M. A. Mahadadalkar, P. S. Alegaonkar, B. B. Kale and S. K. Pardeshi, *Electrochim. Acta*, 2018, **291**, 225–233.

45 J. Chen, C. Lin, M. Zhang, T. Jin and Y. Qian, *ChemElectroChem*, 2020, **7**, 3311–3318.

46 M. Aftabuzzaman, C. K. Kim, T. Kowalewski, K. Matyjaszewski and H. K. Kim, *J. Mater. Chem. A*, 2019, **7**, 20208–20222.

47 T. Ma, M. Zhang, H. Liu and Y. Wang, *Electrochim. Acta*, 2019, **322**, 134762.

48 A. S. Rajpurohit, N. S. Punde, C. R. Rawool and A. K. Srivastava, *Chem. Eng. J.*, 2019, **371**, 679–692.

49 C. K. Kim, H. Zhou, T. Kowalewski, K. Matyjaszewski and H. K. Kim, *ACS Appl. Mater. Interfaces*, 2019, **11**, 2093–2102.

50 C. K. Kim, J. M. Ji, H. Zhou, C. Lu and H. K. Kim, *Nanomaterials*, 2020, **10**, 29.

51 M. J. Ju, I. T. Choi, M. Zhong, K. Lim, J. Ko, J. Mohin, M. Lamson, T. Kowalewski, K. Matyjaszewski and H. K. Kim, *J. Mater. Chem. A*, 2015, **3**, 4413–4419.

52 I.-Y. Jeon, H. M. Kim, I. T. Choi, K. Lim, J. Ko, J. C. Kim, H.-J. Choi, M. J. Ju, J.-J. Lee, H. K. Kim and J.-B. Baek, *Nano Energy*, 2015, **13**, 336–345.

53 M. J. Ju, I.-Y. Jeon, H. M. Kim, J. I. Choi, S.-M. Jung, J.-M. Seo, I. T. Choi, S. H. Kang, H. S. Kim, M. J. Noh, J.-J. Lee, H. Y. Jeong, H. K. Kim, Y.-H. Kim and J.-B. Baek, *Sci. Adv.*, 2016, **2**, e1501459.

54 C. K. Kim, I. T. Choi, S. H. Kang and H. K. Kim, *RSC Adv.*, 2017, **7**, 35565–35574.

55 B. Liu, Q. Zhang, Z. Wang, L. Li, Z. Jin, C. Wang, L. Zhang, L. Chen and Z. Su, *ACS Appl. Mater. Interfaces*, 2020, **12**, 8225–8232.

56 I.-Y. Jeon, H. M. Kim, D. H. Kweon, S.-M. Jung, J.-M. Seo, S.-H. Shin, I. T. Choi, Y. K. Eom, S. H. Kang, H. K. Kim, M. J. Ju and J.-B. Baek, *Nano Energy*, 2016, **30**, 867–876.

57 H. M. Kim, I.-Y. Jeon, I. T. Choi, S. H. Kang, S.-H. Shin, H. Y. Jeong, M. J. Ju, J.-B. Baek and H. K. Kim, *J. Mater. Chem. A*, 2016, **4**, 9029–9037.

58 G. Qu, S. Jia, H. Wang, F. Cao, L. Li, C. Qing, D. Sun, B. Wang, Y. Tang and J. Wang, *ACS Appl. Mater. Interfaces*, 2016, **8**, 20822–20830.

59 R. Soni, V. Kashyap, D. Nagaraju and S. Kurungot, *ACS Appl. Mater. Interfaces*, 2018, **10**, 676–686.